UNIVERSITY OF CALIFORNIA

Santa Barbara

Stress drop and its Uncertainty for Earthquakes M3.8-5.5 in Central California and Oklahoma

A Thesis submitted in partial satisfaction of the

requirements for the degree Master of Science

in Geophysics

by

Luyuan Ding

Committee in charge:

Professor Ralph J. Archuleta, Chair

Professor Chen Ji

Dr. Jamison Steidl

September 2015

The thesis of Luyuan Ding is approved.

_____

Chen Ji

_____

Jamison Steidl

_____

Ralph J. Archuleta, Committee Chair

September 2015

Stress drop and its Uncertainty

for Earthquakes M3.8-5.5 in Central California and Oklahoma

Copyright © 2015

by

Luyuan Ding

ACKNOWLEDGEMENTS

Firstly, I would like to express my sincere gratitude to my advisor Prof. Ralph J. Archuleta for the continuous support of my graduate study and related research, for his patience, motivation, and immense knowledge. His guidance helped me in all the time of research and writing of this thesis. I could not have imagined having a better advisor and mentor for my study.

Besides my advisor, I would like to thank the rest of my thesis committee: Prof. Chen Ji and Prof. Jamison Steidl, for their insightful comments and encouragement, but also for the hard question which incented me to widen my research from various perspectives.

I thank my fellow labmates in for the stimulating discussions, for the sleepless nights we were working together before deadlines, and for all the fun we have had in these years. Also I thank my friends in various institution. In particular, I am grateful to Dr. Jorge Crempien for enlightening me the first glance of research.

Last but not the least, I would like to thank my family: my parents, as well as my friends for supporting me spiritually throughout writing this thesis and my life in general.

ABSTRACT

Stress drop and its Uncertainty

in Central California and Oklahoma Earthquakes M3.8-5.5

by

Luyuan Ding

Stress drop is the stress that is effectively available to drive fault motion. It is a key parameter in predicting peak ground acceleration (PGA), since $PGA \propto \Delta\sigma^{5/6}$, and it is very important in estimating ground motion. However, it is difficult to get an accurate estimation of stress drop. In order to get a more stable measurement of stress drop, we test two methods in this thesis: the first one is the Brune stress drop, which is more commonly applied, and the second one is the A_{rms} stress drop, which less applied before and theoretically should have less uncertainty. By comparing these two methods we would like to test the feasibility and stability of the A_{rms} method. We applied these two methods to data of earthquakes M3-5.5 in California and Oklahoma. We found that, taking Oklahoma results as an example, the mean value of Brune stress drop is 0.38 MPa, with a multiplicative uncertainty of 3.12, and the mean value of A_{rms} stress drop is 1.04, with a multiplicative uncertainty of 1.79. Therefore we concluded that the A_{rms} method is a good estimator of stress drop, with a smaller uncertainty. We determine the path attenuation so that we can increase the source-station distance of events studied to be as

much as 76 km. The path seismic attenuation is a critical parameter that must be included in the analysis.

TABLE OF CONTENTS

1. Introduction

1.1 Stress Drop and Ground Motion

Earthquakes pose a serious threat to many areas in the world among natural hazards such as floods, volcanic eruptions or storms. The April 2015 Nepal earthquake killed more than 9,000 people and injured more than 23,000. Rajiv Biswas, an economist at a Colorado-based consultancy, said that rebuilding the economy will need international effort over the next few years as it could "easily exceed" USD$5 billion, or about 20 percent of Nepal's gross domestic product.

However, it is extraordinarily difficult to assess the current state of a fault zone and forecast an earthquake. An earthquake is a very complex interaction of many different physical parameters that can only be indirectly observed, and the physics of the source process is not completely understood.

Regardless whether or not it will be feasible to provide reliable earthquake predictions, it is important to predict ground shaking (either deterministically or probabilistically, see e.g. Kramer, 1996) from these future earthquakes, in order to assess the potential for seismic damage and hazard. There are many methods for simulating ground motion from earthquakes (see Schmedes et al., 2013; Graves and Pitarka, 2010; Mena et al., 2010, Irikura and Miyake, 2010; Zeng et al., 1994 and citations within). A common feature of all of these methods is that the high-frequency ground motion is related to the stress drop during the earthquake. Stress drop (stress parameter) also usually serves as a typical input parameter in the simulation methods using the stochastic technique.

What's more, among ground motion parameters, peak ground acceleration (PGA) is a commonly used ground motion parameter in earthquake engineering (Kramer, 1996). Cotton et al. (2012) show that PGA and stress drop ($\Delta\sigma$) have a proportional relation, $PGA \propto \Delta\sigma^{5/6}$. With a more precise and stable measurement of stress drop we can get a more precise and stable estimate of PGA.

Strictly speaking, stress drop is distinguished between static stress drop and dynamic stress drop. Static stress drop is defined as the (static) difference between the shear stress on the fault before and after the earthquake. It gives information on the scaling of the static parameters (such as fault size or final displacement) of the earthquake. Dynamic stress drop is the stress that is effectively available to drive fault motion. It is a key parameter in the estimation of strong ground motion, as it influences the high-frequency level of acceleration (Brune, 1970, 1971). Moreover, it is the dynamic stress drop that is linked to peak ground acceleration (PGA, Hanks and Johnson, 1976; Cotton et al., 2012). The stress drop in this thesis refers to dynamic stress drop.

As with some other source parameters, stress drop could be derived from the spectra of seismic waves (Brune, 1970). The most commonly determination of stress drop follows Brune (1970) where the Fourier amplitude spectrum (FAS) is used to determine corner frequency (f_C) and a low-frequency asymptote that is related to seismic moment (M_O). With these two parameters, the stress drop (Brune) can be determined:

$$\Delta\sigma_B = \frac{7M_O}{16}\left(\frac{2\pi f_C}{2.34\beta}\right)^3 \tag{1.1}$$

The method will be amply treated in Section 1.2. This approach has a strong dependence on f_C . If there is much error in determining f_C , then the uncertainty in stress drop result ($\Delta\sigma_B$) can be large. A relative error of 10% in corner frequency will

lead to 30% relative error in stress drop. Recent source studies show that it has a multiplicative uncertainty of the mean stress drop is between 4.0 to 5.5. (Figure 1.1) (Cotton et.al 2012). In Log units, the standard deviation is 0.60-0.74.

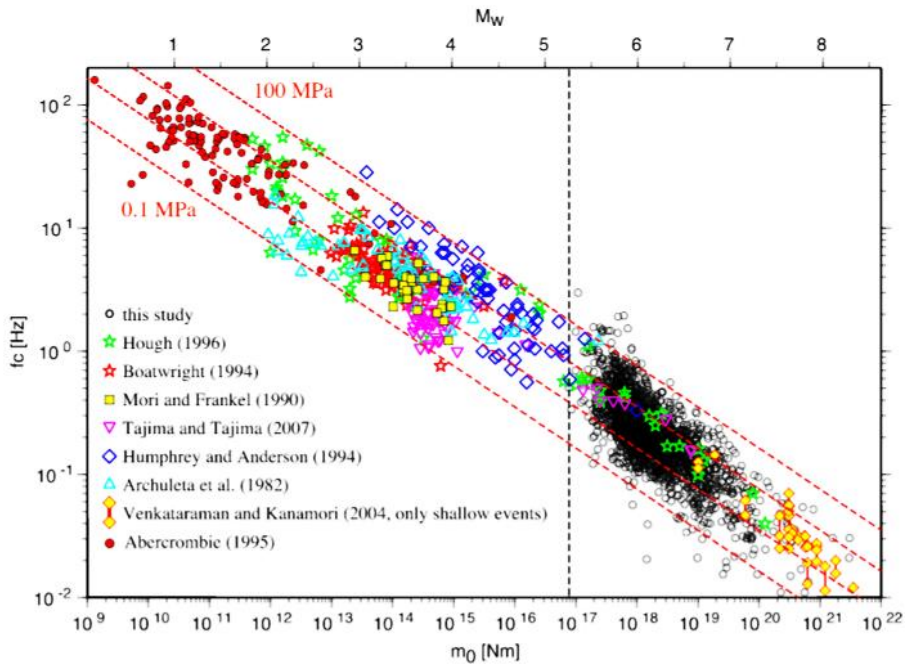

Figure 1.1: Plot of corner frequency vs seismic moment, from Allmann and Shearer (2009). Note that at any seismic moment the range of stress drops is about three orders of magnitude.

As discussed above $PGA \propto \Delta\sigma^{5/6}$; hence the uncertainty in the stress drop should be 5/6 times the uncertainty in PGA. However, the uncertainty of recent source studies (Allmann and Shearer, 2009 and references herein) have a variability that is, roughly 2-3 times larger than the variability implied by the GMPEs (Cotton et al, 2012). We assume that the intrinsic variability of stress drop may be smaller; the large uncertainty is due to the uncertainty in estimating corner frequency. So we are seeking a more stable method to estimate stress drop.

Hanks (1979) related earthquake stress drop to the root-mean-square value of acceleration time histories (A_{rms}) beginning at the S-wave arrival, for close distances,

$$\Delta\sigma\text{-A}_{rms} = A_{rms}\frac{106\rho R}{2R_{\theta\varphi}(2\pi)^2}\sqrt{\frac{f_C}{f_{\max}}} \qquad (1.2)$$

$f_{\max}$ marks the high frequency after which the acceleration Fourier amplitude spectrum decays from a nearly constant level, $R_{\theta\varphi}$ is the radiation pattern, and R is the source-site distance. We will discuss more details of this method in Section 1.3. As shown in Equation1.2, 10% f_C uncertainty will only lead to 5% relative error in stress drop. Theoretically it seems that we could eliminate part of the error in f_C and therefore find a more stable method to estimate stress drop (and PGA).

What's more, the attenuation that occurs along the seismic wave path can greatly affect the S-wave amplitude spectrum. Hence it will affect both the Brune and A_{rms} stress drop estimate. We need to find a solution that eliminates this path effect. Section 1.4 introduces the basic ideas and a method to remove the effect of path attenuation. This is necessary in order to reduce errors and to enlarge the hypocentral distance of events that we are studying.

In this study, we test the feasibility of the A_{rms} method to serve as the more stable method to estimate stress drop. We compare the A_{rms} stress drop and Brune stress drop for magnitude 3.8-5.5 earthquakes in central California and magnitude 3.0-4.0 earthquakes in Oklahoma. All spectra are corrected for path attenuation (Q). The objective is to find a more stable method to estimate stress drop, thus we might make better ground motion predictions. This will also allow us to test the A_{rms} stress drop as a better seismological source parameter than the Brune stress drop.

1.2 Brune stress drop

It is found that the ω^{-2} model is the best to explain observed seismogram spectra (Aki, 1967; Brune, 1970). In a general form, the ω^{-2} model for theoretical source displacement Fourier amplitude spectrum (FAS) can be written as:

$$\left|S\left(x, f\right)\right| = \Omega_O \cdot \left[1 + \left(\frac{f}{f_C}\right)^2\right]^{-1} \tag{1.3}$$

The formula describes a spectrum that has the following three characteristics: 1) a flat portion (with a limiting value of Ω_O as f goes to zero) at low frequencies ($f < f_C$); 2) a turning point near $f = f_C$ where the amplitude begins to decay; 3) a spectral decay proportional to f^{-2} for high frequencies ($f > f_C$).

According to the properties of Fourier transformation, we could imply that the velocity spectrum will be firstly increasing proportional to f^1 ($f < f_C$), and then decaying proportional to f^{-1} ($f > f_C$). The acceleration spectrum will first be increasing proportional to f^2 ($f < f_C$), and then it will have a constant level segment ($f > f_C$). All of this is for no attenuation, $Q = \infty$. The shapes of the Fourier amplitude spectrum are shown in Figure 1.2.

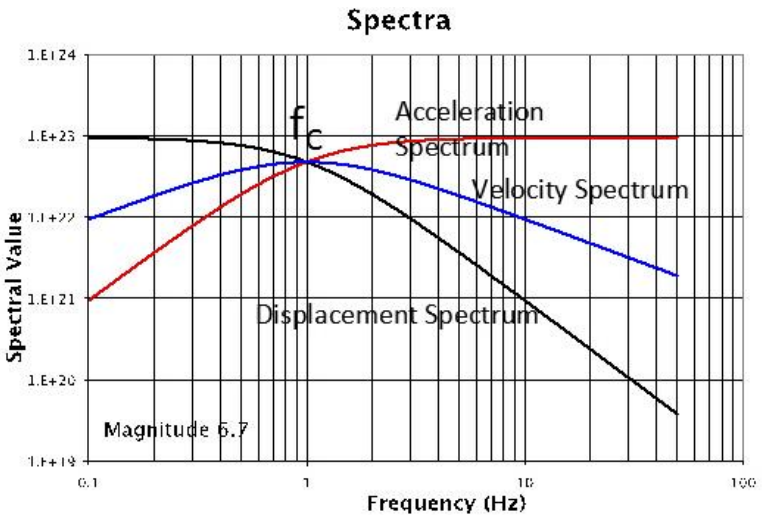

Figure 1.2: Idealized FAS shapes of the S-wave.

Therefore, the FAS of the source, for example the one shown in Figure 1.2, could be parameterized into corner frequency f_C (the intersection between the low-frequency plateau and the f^{-2} decaying part of the displacement spectrum), Ω_O (displacement low-frequency level). We can find these parameters by nonlinear least squares fitting of Equation (1.3) to the observed spectrum.

Particularly, there will be a parameter called $f_{\max}$ which means the cut-off frequency due to path attenuation. It defines the frequency at which the amplitude of acceleration spectrum ($f > f_C$) begins to decay. We can use this part of the spectrum to estimate the attenuation in the path, discussed in Section 1.4.

Brune (1970, 1971) assumes a circular fault with a radius of r and no specific directivity (Figure 1.3), on which an instantaneous shear stress pulse is applied. This stress pulse generates a shear wave that propagates through the medium at a speed of β.

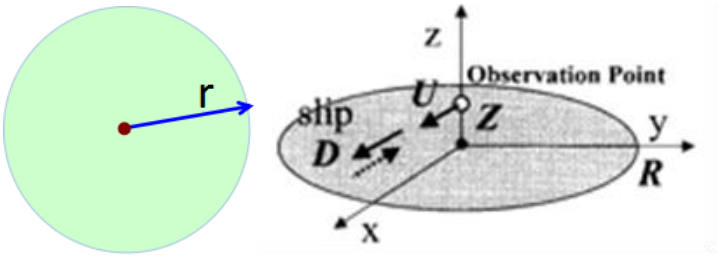

Figure 1.3: Plan view and 3D view of a circular fault geometry.

As the stress pulse is applied instantaneously, we could assume that there is no effect of rupture propagation. The far-field displacement in this model is given by:

$$u(t) = R_{qj}\,\frac{r}{R}\cdot\frac{\Delta\sigma}{m}\,b\left(t-\frac{R}{b}\right)e^{-2\pi f_C\left(t-\frac{R}{b}\right)} \tag{1.4}$$

where $R_{\theta\varphi}$ is the radiation pattern, r is the fault radius, R is the source-site distance, r/R corresponds to a geometrical attenuation term, $\Delta\sigma$ is the (dynamic) stress drop, μ is the shear modulus, β is the shear wave speed. After Fourier transforming to the frequency domain, the FAS of displacement is given by (easily seen that it has the ω^{-2} ($w = 2\pi f$) shape at high frequencies):

$$|u(f)| = R_{\theta\varphi}\,\frac{r}{4\pi^2 R}\cdot\frac{\Delta\sigma}{\mu}\,\beta\,\frac{1}{f^2 + f_C^{\,2}} \tag{1.5}$$

with,

$$f_C = \frac{2.34}{2\pi}\cdot\frac{\beta}{r} \tag{1.6}$$

Equation 1.6 is the very famous relation that links the spectral parameter corner frequency f_C to the dimension of source as radius r (Brune, 1970, 1971). It has been numerously applied for estimating source dimensions from the study of FAS.

Finally, Equation (1.6) relation together with Eshelby's relation between moment and radius, leads to the following relation between the seismic moment and the stress drop:

$$\Delta\sigma_B = \frac{7M_O}{16}\left(\frac{2\pi f_C}{2.34\beta}\right)^3 \tag{1.7}$$

Equation (1.7) assumes total stress drop, i.e. the shear stress drops from the tectonic stress σ_0 to the frictional stress σ_f. Boatwright (1984) shows that the Brune stress drop is correlated with dynamic stress drop rather than with average static stress drop Thus Brune stress drop estimates dynamic stress drop rather than static stress drop. This is in accordance with the initial assumption and formulation of the Brune model.

So we can estimate stress drop by finding corner frequency f_C and seismic moment M_O, Equation (1.7).

The corner frequency f_C is found by fitting the FAS. There are two different ways to get M_O. One way is to use the least squares fit to the low-frequency asymptote of the displacement spectrum to determine Ω_0, from which seismic moment can be found:

$$M_O = \frac{4\pi\rho\beta^3 R\Omega_0}{R_{\theta\varphi}} \tag{1.8}$$

The other way is to use the magnitude from the catalog and convert it to the moment magnitude scale (Hanks and Kanamori, 1979):

$$\boldsymbol{M} = \frac{2}{3}\log_{10} M_O\left[Nm\right] - 6.03 \tag{1.9}$$

We assume that there is not much difference among different methods of estimating event magnitude such as $\boldsymbol{M}$, M_l and $M_{b-\lg}$, etc. It is not clear which method is better to determine seismic moment M_O. An advantage of the latter is that magnitude from the

catalog is an average of multiple records with various locations. In this study, we use both methods and compare their accuracy and stability, especially for the dataset at Oklahoma. Results are shown in Chapter 3.

1.3 A-rms stress drop

Hanks (1979) proposed the A_{rms} method derived from the Parseval's Theorem, which states that the energy in the time domain is equal to the energy in the frequency domain. Therefore the acceleration time series and its FAS has the following relation (following Hanks, 1979, equation 10),

$$\int_{-\infty}^{\infty}\left|a(t)\right|^2 dt = \frac{1}{2\pi}\int_{-\infty}^{\infty}\left|\tilde{a}(\omega)\right|^2 d\omega = \frac{1}{\pi}\int_{0}^{\infty}\left|\tilde{a}(\omega)\right|^2 d\omega \qquad (1.10)$$

It is assumed that the energy of the event in time series is enclosed within a time window with a length of the duration of faulting Td, starting from the arrival of significant motion (referred as t=0) in seismogram. Then the left part of equation can be rewritten as,

$$\int_{-\infty}^{\infty}\left|a(t)\right|^2 dt \approx \int_{0}^{T_d}\left|a(t)\right|^2 dt \qquad (1.11)$$

And as discussed above in Section 1.2, the FAS of acceleration theoretically has a ω^{-2} shape which will increase proportional to f^2 ($f < f_C$), and then having a flat (constant) portion ($f > f_C$). We assume the energy in low frequency part ($f < f_C$) is negligible. What's more, practically the flat portion at high frequencies ($f > f_C$) will not be flat after a cut-off frequency $f_{\max}$ due to path attenuation. Thus we also neglect the energy in high frequency part ($f > f_{\max}$). Therefore the right part of equation can be rewritten as,

$$\frac{1}{\pi}\int_0^{\infty}\left|\tilde{a}(\omega)\right|^2 d\omega \approx \frac{1}{\pi}\int_{2\pi f_C}^{2\pi f_{\max}}\left|\tilde{a}(\omega)\right|^2 d\omega \tag{1.12}$$

Combine equations (1.10) to (1.12) we will get, (Hanks, 1979, equation 11),

$$\int_0^{T_d}\left|a(t)\right|^2 dt = \frac{1}{\pi}\int_{2\pi f_C}^{2\pi f_{\max}}\left|\tilde{a}(\omega)\right|^2 d\omega \tag{1.13}$$

For FAS of source displacement following a Brune (1970) model,

$$\left|\tilde{a}(\omega)\right| = 2\frac{1}{\sqrt{2}}R_{\theta\varphi}\frac{\Omega_0}{1+(\omega/\omega_C)^2} \tag{1.14}$$

Where Ω_0 is the low frequency plateau level of the displacement spectrum, proportional to seismic moment M_O. The factor of 2 accounts for free surface amplification; the factor of $1/\sqrt{2}$ accounts for partitioning of ground motion onto two horizontal components; $R_{\theta\varphi}$ is the shear-wave radiation pattern. Therefore, using properties of Fourier transform, the high frequency plateau level of acceleration FAS ($f_C < f < f_{\max}$) can be written as (Hanks, 1979, his equation 13),

$$\left|\tilde{a}(\omega)\right| = \sqrt{2}R_{\theta\varphi}\Omega_0\omega_C{}^2 = \sqrt{2}R_{\theta\varphi}\Omega_0(2\pi f_C)^2 \tag{1.15}$$

The definition of A_{rms}, the root mean square of acceleration, over the interval [0, Td] is (Hanks, 1979, his equation 12),

$$A_{rms} = \sqrt{\frac{1}{T_d}\int_0^{T_d}\left|a(t)\right|^2 dt} \tag{1.16}$$

Combining Equations (1.13) (1.15) and (1.16), with the assumption that $f_{\max} >> f_C$, so that $f_{\max} - f_C \approx f_{\max}$, we get,

$$A_{rms} = \sqrt{\frac{1}{T_d}\frac{1}{\pi}\int_{2\pi f_C}^{2\pi f_{\max}} \left|\tilde{a}(\omega)\right|^2 d\omega}$$
$$= \sqrt{\frac{1}{T_d}\frac{1}{\pi}\left|\sqrt{2}R_{\theta\varphi}\Omega_0(2\pi f_C)^2\right|^2 (2\pi f_{\max} - 2\pi f_C)} \quad (1.17)$$
$$= 2R_{\theta\varphi}(2\pi)^2\Omega_0 f_C{}^3 \frac{1}{f_C}\sqrt{\frac{f_{\max}}{T_d}}$$

As stress drop is related to Ω_0 for the Brune ω^{-2} model (Hanks and Thatcher, 1972),

$$\Delta\sigma = 106\rho R\Omega_0 f_C{}^3 \quad (1.18)$$

Combining Equations (1.17) and (1.18) gives,

$$\Delta\sigma_{A_{rms}} = A_{rms}\frac{106\rho R}{2R_{\theta\varphi}(2\pi)^2} f_C\sqrt{\frac{T_d}{f_{\max}}} \quad (1.19)$$

Equation (1.19) expresses A_{rms} stress drop $\Delta\sigma_{A_{rms}}$ in terms of A_{rms}, $f_{\max}$, f_C.

We also try to directly compute $\left|\tilde{a}(\omega)\right|$ from the acceleration spectrum. We take the average spectral level from a frequency that is greater than the corner frequency f_C up to a maximum frequency where the acceleration spectrum is mostly flat ($f_C < f < f_{\max}$). Since it has the following relation,

$$A_{rms}{}^2 = \frac{2(f_{\max} - f_C)}{T_d}\left|\bar{a}(\omega)\right|^2 \quad (1.20)$$

Combining Equations (1.19) and (1.20), we find,

$$\Delta\sigma_{A_{rms}} = \left|\bar{a}(\omega)\right|\frac{106\rho R}{\sqrt{2}R_{\theta\varphi}(2\pi)^2} f_C \quad (1.21)$$

We will test the feasibility and stability of this method (Equation (1.21)) especially with the dataset in California, taking Td as $1/f_C$. Results are presented in Chapter 2. Section 3.

In particular, there are three points in our method that differ from the original A_{rms} method (Hanks, 1979):

1) We test different lengths of duration of faulting Td; we use 1.0 s and 1.5 s. These durations are based on the event magnitudes in this study are around 3-4.5. We do not simply use $T_d = 1/f_C$ because there can be an error in f_C. Sometimes the f_C is as big as 4 Hz meaning that the time window of $1/f_C$ will be too short to get an accurate A_{rms}. We hope this even simpler way may reduce the final error. Results could be seen in analysis of Oklahoma data in Chapter 3.3;

2) The A_{rms} we are using is not from the raw accelerogram, but from the inverse Fourier transform of the spectrum after correcting it for attenuation. The steps are as follows: (i) Fast Fourier Transform (FFT) the acceleration seismogram; (ii) correct for the FAS for Q; (iii) inverse Fast Fourier Transform (Ifft) the corrected FAS to the produce a new time-domain accelerogram. With this new accelerogram compute A_{rms} using durations of 1.0 s and 1.5 s. By doing this we hope to increase the accuracy of A_{rms} and allow for events with longer source-site distances. We increase the distance from 20 km of previous studies to 80 km.

3) We use different values for $f_{\max}$ after we correct for path attenuation Q. Recall that $f_{\max}$ is chosen as the frequency where the high frequency acceleration spectrum is no longer constant. After we corrected for Q the flat part of the spectrum will extend to a larger frequency. Ideally it would go to infinity, but that does not happen due to high-frequency noise. Further details can be seen in Chapter 1, Section 4.

The A_{rms} method has the following advantages: 1) A_{rms} stress drop is proportional to the square root of f_C, so any error in f_C produces a smaller error in A_{rms}.; 2) By

knowing some simple and easily measured parameters such as corner frequency f_C, cut-off frequency $f_{\max}$, and acceleration root-mean-square A_{rms}, we can estimate the stress drop.

However, A_{rms} stress drop is not widely applied as a seismology source parameter aside of its application to ground-motion prediction. So in this study, by comparing A_{rms} stress drop and Brune stress drop, we aim to help renew its importance as being a basic source parameter in the source studies. What's more, by doing the modifications we discussed above, we aim to optimize this method.

1.4 Path attenuation

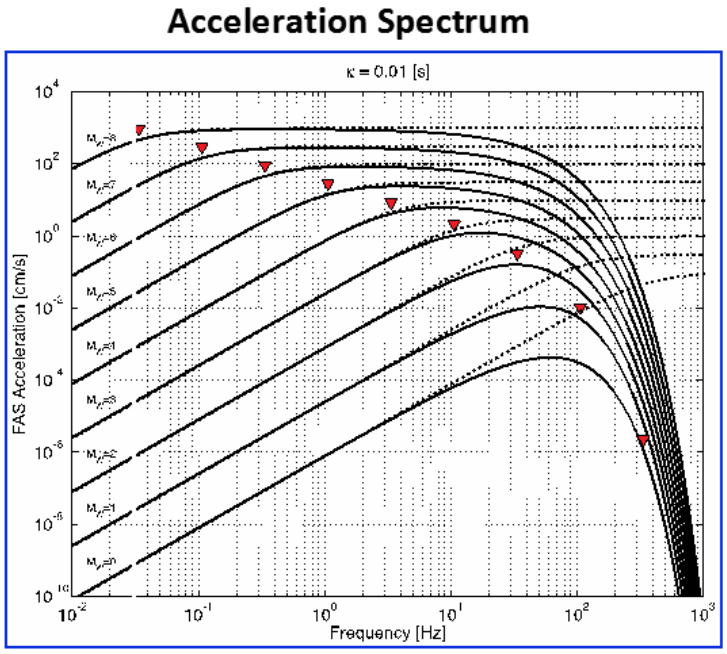

Figure 1.4: FAS acceleration spectra for various magnitudes. The dotted lines are the theoretical spectra. The solid lines are the spectra has modified by an attenuation e^{-pfk} where $k = 0.01s$. Red triangles are the corner frequency. As seen, the corner frequency is inaccurate for magnitudes less than 6 when k of 0.01 s. Typical values of k in the western US are more like 0.03-0.04 s. $k = T_t / Q$ where T_t is the travel time between source and station of the S wave and Q is seismic attenuation.

As seen in Figure 1.4, path attenuation (Q) strongly affects the acceleration spectrum at high frequencies. For small events, the spectrum may decay even before it reaches corner frequency f_C; this will lead to larger errors in corner frequency f_C (e.g., Anderson, 1986). So it is important to find a way to correct for the Q effect in order to estimate a stable and accurate stress drop.

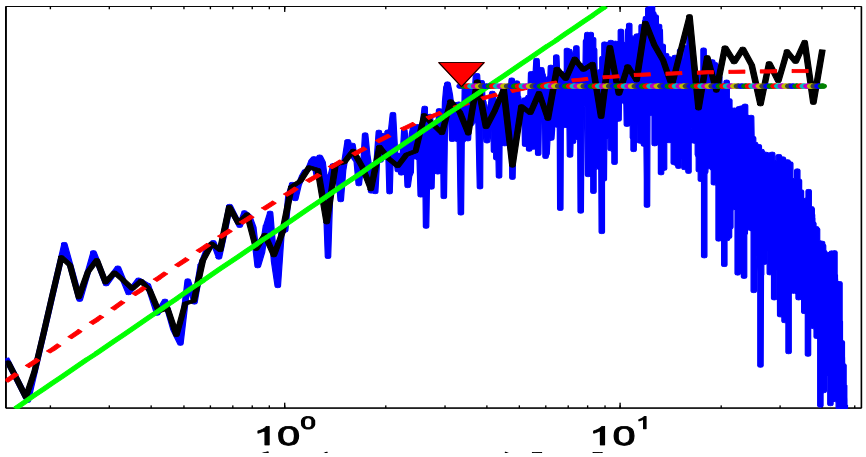

Figure 1.5: Example of FAS of acceleration before and after removing path effect. Blue line is the original FAS; black line is the FAS after correcting for Q. Red dashed line is the least squares fit to the spectrum after correcting for Q. Green line is the level of acceleration based on the catalog magnitude. Red triangle is the location of the corner frequency.

Figure 1.5 shows the difference that removing path attenuation can make, especially in detecting f_C.

In order to eliminate Q effect, we trace it back to the origin: the equation of motion and its FAS. We assume that the S-wave seismogram - the displacement spectrum of the earthquake at the station may be expressed as a product of a source, propagation, and site term in the frequency domain.

$$U(f) = S(f)\cdot P(f)\cdot O(f) \qquad (1.22)$$

$S(f)$, $P(f)$ and $O(f)$ represent source, propagation and site terms, respectively. This becomes a sum in the logarithm domain:

$$\log U(f) = \log S(f) + \log P(f) + \log O(f) \tag{1.23}$$

We assume propagation may be described by simple spreading and attenuation function, of the form,

$$P(f) = \frac{1}{R} e^{- Rgf}, g = \frac{p}{bQ} \tag{1.24}$$

where R is hypocentral distance, β is the shear velocity, and Q is a single, regionally averaged quality factor that is seismic Q.

Substituting equation (1.24) into equation (1.23) yields the linear equation describing a single measurement,

$$\log U(f) = \log S(f) - \log(R) - \left(\frac{g}{2.3} \right) Rf + \log O(f) \tag{1.25}$$

In this study we use a Q model of $Q = Q_0 f^{\alpha}$ for all earthquakes. In addition, there is an unknown absolute scaling for all seismograms (e.g., from counts to ground displacement) and for the size of each earthquake that is independent of frequency. These can be combined into a single unknown, Cj , for each source. Equation (1.25) becomes,

$$\log U(f) + \log(R) = Cj - \left(\frac{pR}{2.3bQ_0} \right) f^{1-a} + \log O(f) \tag{1.26}$$

Mathematically, we can solve for Q_0 and a for each observation record fitting a form of $y = a + bf^{1-a}$.

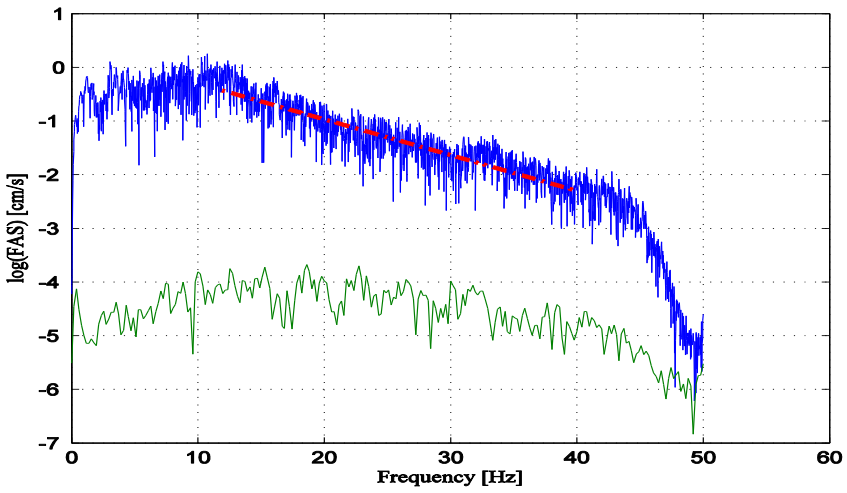

Figure 2: Finding Q from the spectrum. The FAS is plotted on a log amplitude vs linear frequency (constant slope will be exponential form). The green spectrum is the noise spectrum. The blue spectrum is the FAS of the S wave. The dashed red line is the best fit to the high-frequency decay of the spectrum beyond the assumed corner frequency. This fit allows us to determine the Q for this path.

$$Q_0 = \frac{-T_t p}{slope} \tag{1.27}$$

$$t^* = -\frac{slope}{\pi} \tag{1.28}$$

Here T_t is the travel time of the S wave from the source to receiver; *slope* is b in the form $y = a + bf^{1-a}$. From this we find $Q = Q_0 f^a$ to correct the spectrum for path attenuation. Note that the correction involves changing the sign of the exponent in equation (1.24). Thus in Figure 5 we would be multiplying the original spectrum by e^{Rgf} to get a corrected spectrum. By doing this, the determination of f_C is more stable, as well as the determination of Ω_0; thus we have a smaller error in the estimate of stress drop. To get to the time domain we transform the corrected FAS while keeping the phase

the same. The acceleration root mean square A_{rms} is then determined by summing the squares of acceleration (point by point) over a duration T_d.

2. Central California Earthquakes

2.1 Stations and Data

We will compare the two methods—Brune and Hanks—using earthquakes recorded at the Hollister Earthquake Observatory (HEO) operated by University of California, Santa Barbara. At the HEO main station accelerometers are located at 192, 110, 50, 20, 10, and 0 meters depth, going from crystalline rock at the bottom, up through consolidated and unconsolidated alluvium to the surface. (Figure 2.1) We only use data from the192m borehole station, which is in the bedrock and uncontaminated from the near surface soil layers.

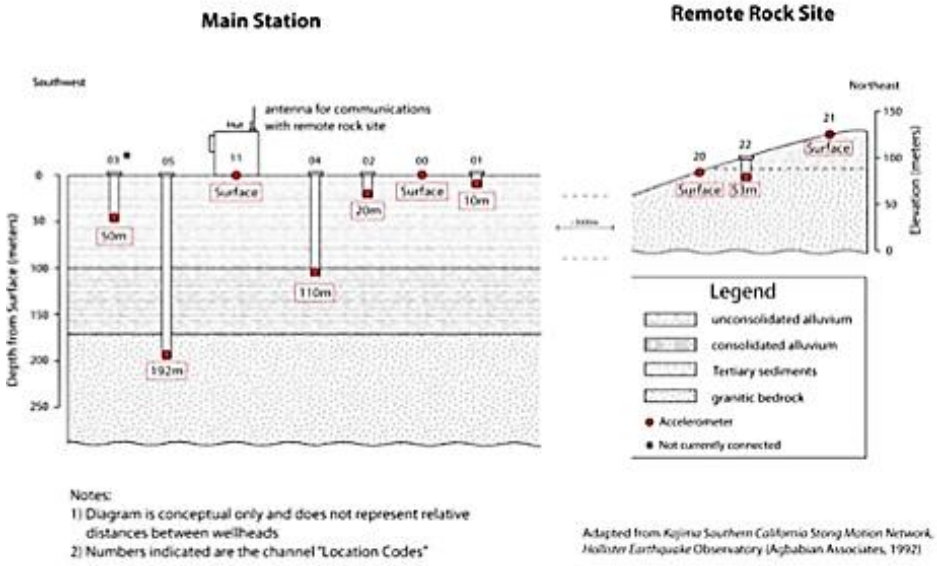

Figure 2.1: Map of the Hollister downhole array. A vertical cross section showing the depths of accelerometers at HEO including a rock site about 3 km from the main array.

We examine earthquakes M>3.8 within a distance of 20 km of HEO and larger earthquakes (M>4.5) within a distance of 100 km recorded in the period January 2001 to January 2013. This results in 14 earthquakes in central California (Figure 2.2)

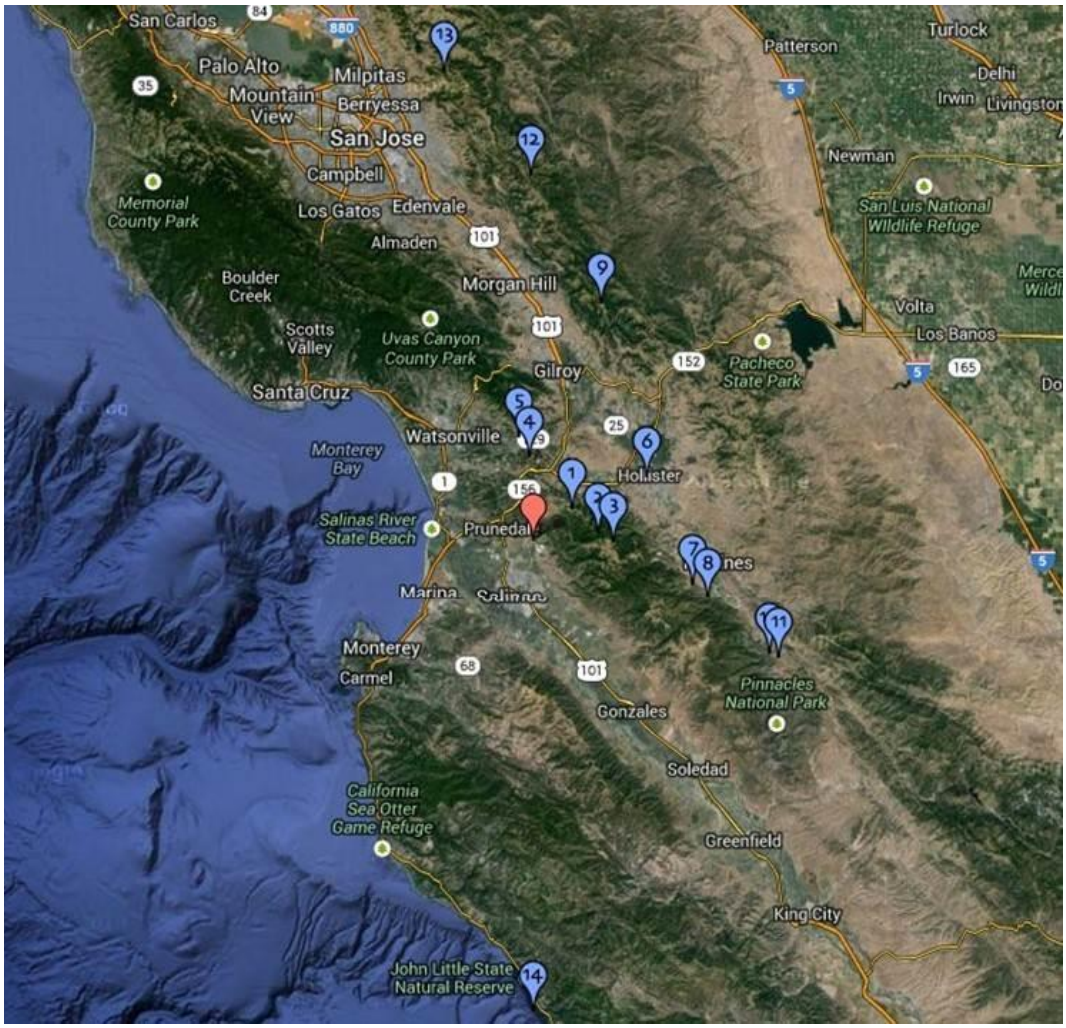

Figure 2.2. Map of epicenters of earthquakes to be analyzed: numbers show the identifier of earthquake events as listed in Table 1.

2.2 Method

We assume a frequency-dependent Q model for path attenuation. To find a regional Q_0 we fit the acceleration amplitude spectrum of the recorded S wave for each earthquake. We examine all 14 earthquakes to determine the mean value of the Q_0. This attenuation is used to remove path attenuation from the spectrum for each earthquake. After correcting for Q we fit each spectrum to a Brune model to determine the low-frequency asymptote and corner frequency. We use the low-frequency

asymptote to determine the seismic moment. With the seismic moment and corner frequency we use Equation (1.1) to estimate stress a Brune stress drop..

The steps in the this approach are as follows:

(1) We isolate the SH time history recorded on the 192 m borehole accelerometer. In steps, we remove the instrument response from the borehole data, remove the trend and convert from counts to physical units. Then we rotate the horizontal components to get the transverse (SH) component based on the epicenter of the earthquake. Next we isolate the shear wave. The length of the time window depends on the specific shape of the SH wave (Figure 2.3a). Next we apply a cosine taper of 0.5% to the isolated waveform to smoothly decrease the amplitude to zero at both ends of the waveform.

(2) We calculate radiation pattern of each event based on the focal mechanism of the USGS and the formulas in Aki and Richards (1980).

(3) We calculate Q for the path using borehole data, which is minimally contaminated by the near surface reflection effect. In this step, we Fourier Transform (FT) the tapered data, plot the spectrum in the log(A)-f format (log-linear), and find a curve that fits this plot using the equation $y = a + bf^{1-a}$ This method is discussed in Chapter 1, Section 3. Then we use the slope value (b) and travel time value to calculate Q_0 and α.

(4) We correct amplitude spectrum for path attenuation using results from step (3).

(5) We fit the corrected source spectrum with a function that is the idealized Brune spectrum to find the corner frequency and low-frequency asymptote. We calculate the Brune stress drop using Equation (1.1).

(6) We determine the A_{rms} by averaging the acceleration spectrum between f_C and $f_{\max}$. We determine the stress drop based on the A_{rms} method, Equation (1.21).

Here, we use tau_fc to represent the Brune method stress drop, and tau_arms as the arms method stress drop.

2.3 Results and Discussion

Table 1 shows the preliminary results of Q_0, alpha, corner frequency (f_C), stress drop from both the Brune method (tau_fc) and the A_{rms} method (tau_arms) for the 14 earthquakes in central California. Mag, Date, and Dist are the magnitude, event date and time, and the epicentral distance of the event from the USGS catalog. M_0 and $\boldsymbol{M}$ are the seismic moment and corresponding moment magnitude calculated from the spectrum of the SH component. Figure 2.3 shows the seismogram and spectra of SH wave component for all 14 events.

Table 1: Path and Source Parameters for earthquake in Central California

ID	Mag	Date Time (UTC)	Dist	M	Qo	alpha	fc	tau_fc	tau_arms
1	3.92	2011/1/13 4:00	8.08	4.11	39.4	0.145	2.54	6.13	5.52
2	4.5	2011/1/12 8:51	10.5	4.08	85.1	0.103	1.87	2.16	2.05
3	3.87	2013/6/28 3:52	12.7	3.7	51.6	0.241	2.89	2.16	2.45
4	4.2	2007/7/2 19:58	13.6	3.89	89.4	0.158	4.15	12.2	11.2
5	3.85	2010/8/10 0:51	17	3.72	94.2	0.146	1.35	0.236	0.22
6	3.87	2009/9/6 9:47	20.8	4.06	48.6	0.222	3.62	14.8	13.4
7	3.9	2009/1/20 6:06	26.4	3.79	93.6	0.287	1.65	0.553	0.572
8	4	2008/12/21 17:35	29.4	3.79	56.2	0.382	4.98	15	13.7
9	4.3	2009/3/30 17:40	39.7	4.22	81.7	0.196	2.66	10.1	9.18
10	3.94	2012/10/29 4:25	41.1	4.15	75	0.432	1.95	3.18	4.2
11	4.64	2011/8/27 7:18	43.1	4.43	42.8	0.513	2.44	16.1	14.6
12	4.3	2009/3/30 17:40	58.7	4.86	47.4	0.097	1.81	29.8	27.6
13	3.89	2013/8/1 1:05	76.3	4.04	33.2	0.32	1.55	1.08	1.2
14	5.45	2007/10/31 3:04	76.5	5.06	130	0.281	1.21	17.4	16.6

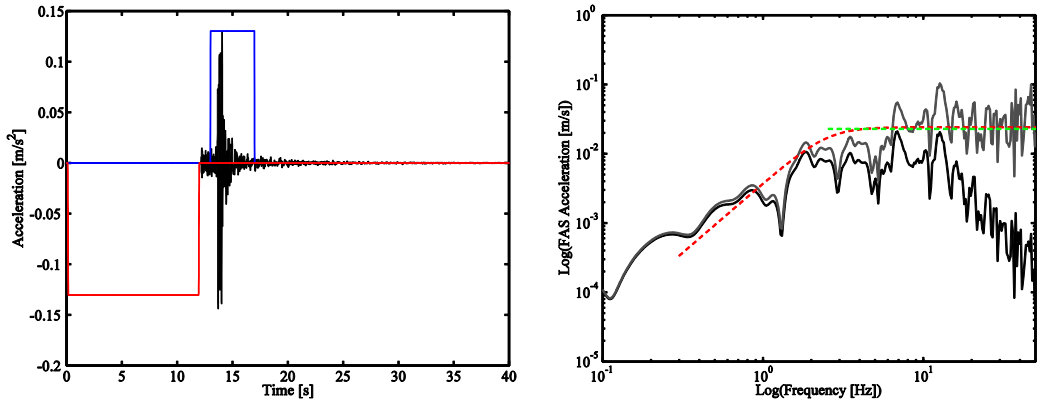

ID 1

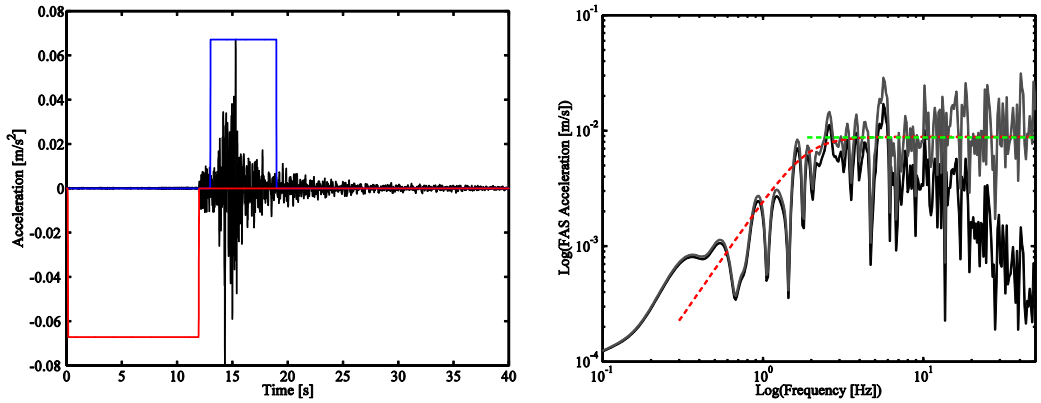

ID 2

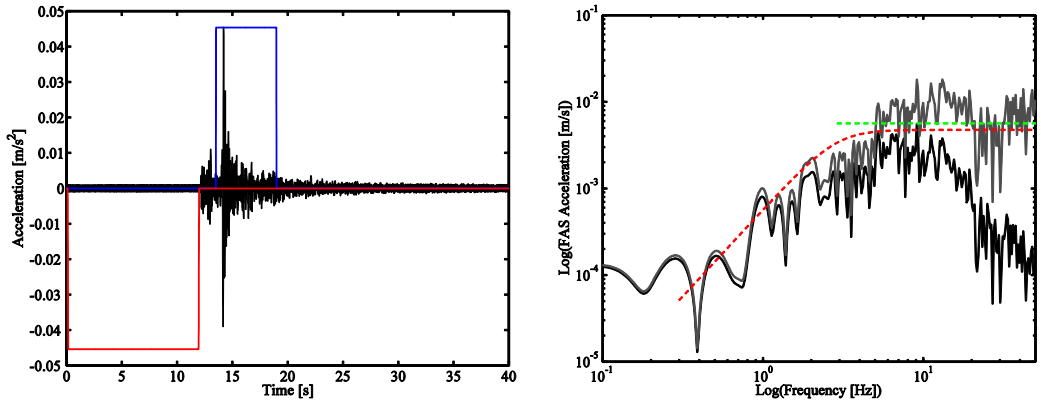

ID 3

Figure 2.3a: seismogram and spectra of S wave.
(a): the seismogram is the transverse component of the earthquake, the blue time window shows the window we use to isolate the SH wave, and the red time window is the one we use to isolate noise, which we use to compare the s/n in spectrum domain.
(b): the black spectrum is the original SH spectrum, and the gray spectrum is the corrected spectrum after we get Q value. The red dash line is the ideal Brune model we fit for the corrected data, and the green dash line is the level we fit for moment on the flat part.

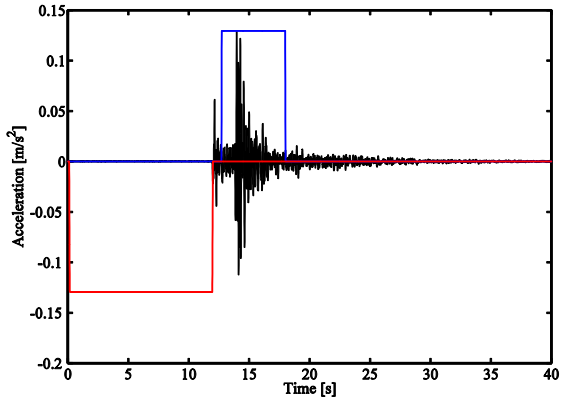

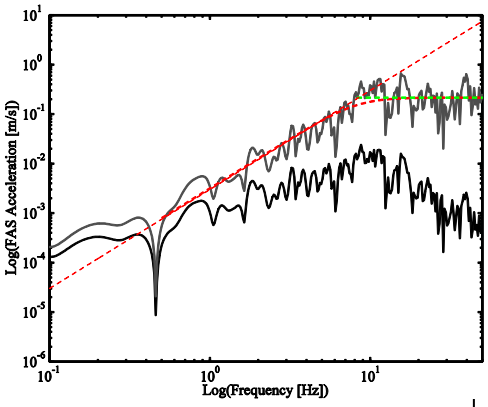

ID 4

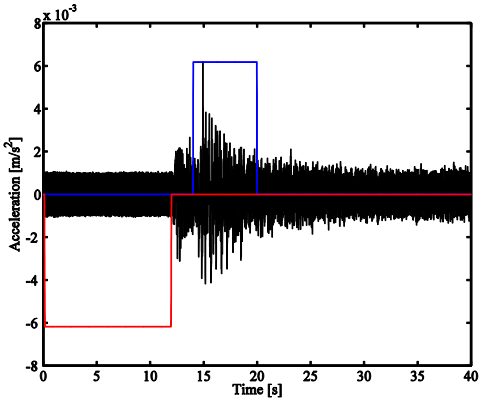

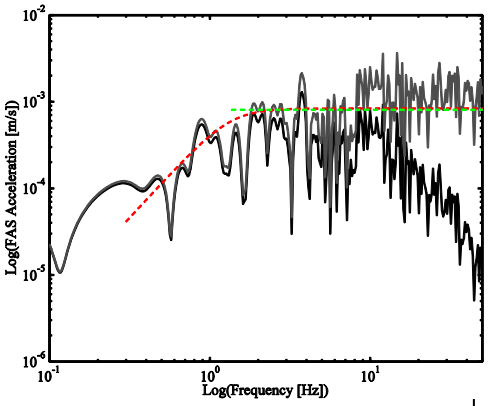

ID 5

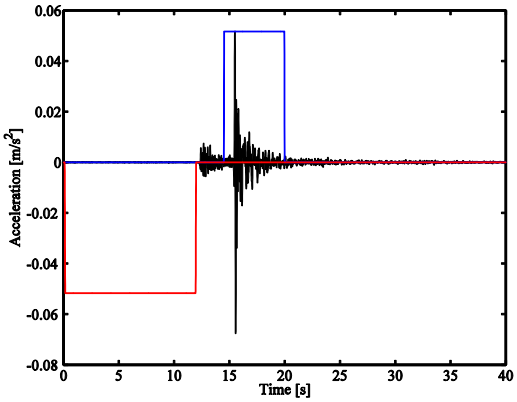

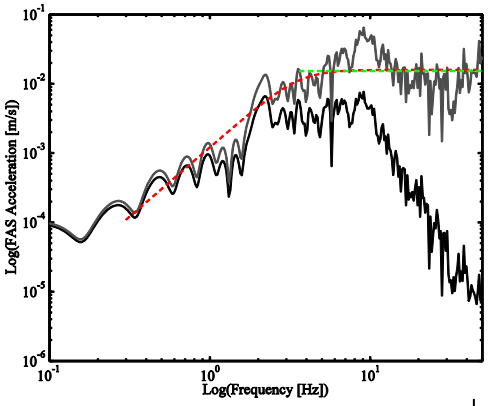

ID 6

Figure 2.3b. figure caption see Figure 2.3a.

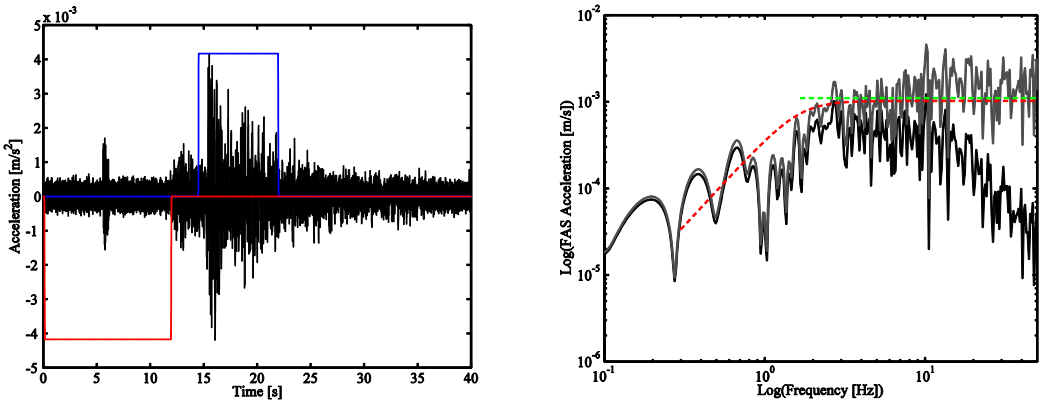

ID 7

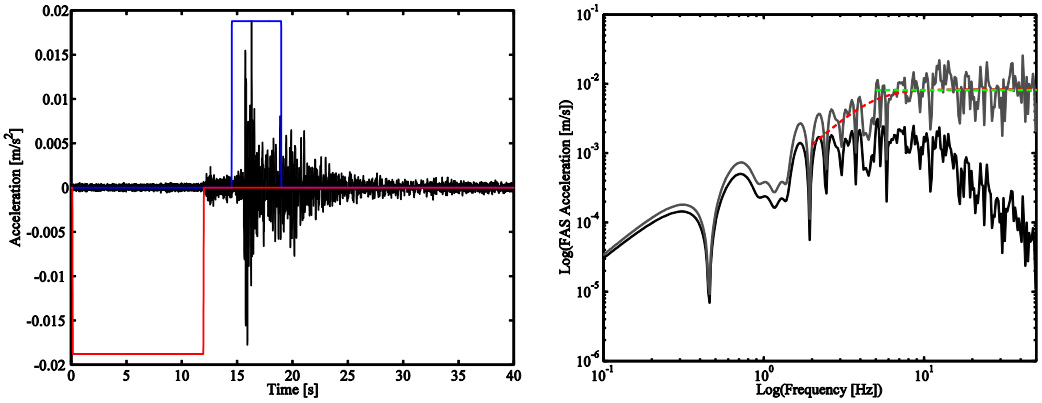

ID 8

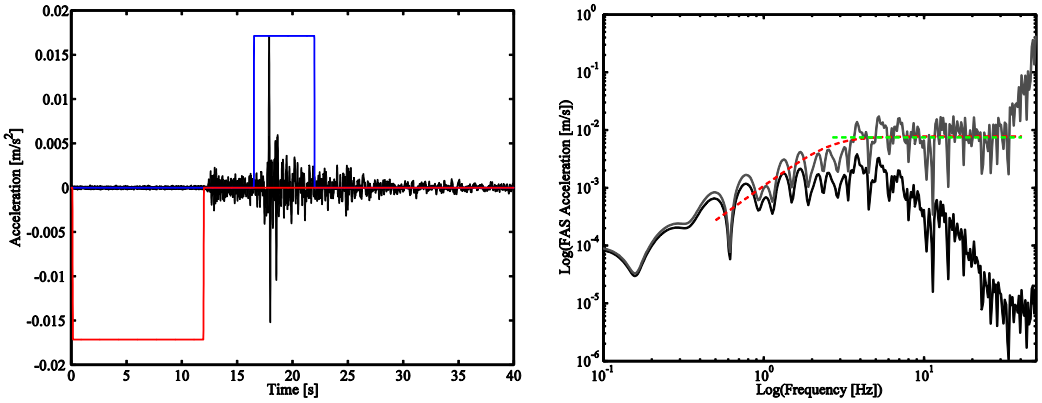

ID 9

Figure 2.3c. figure caption see Figure 2.3a.

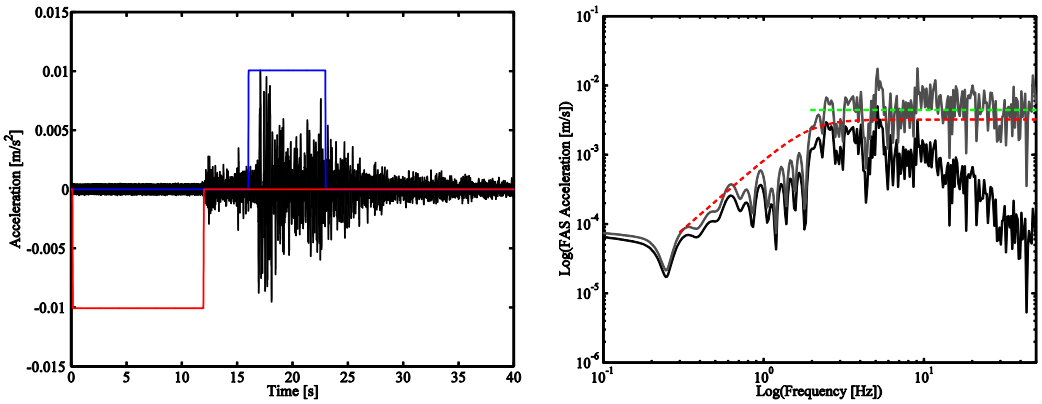

ID 10

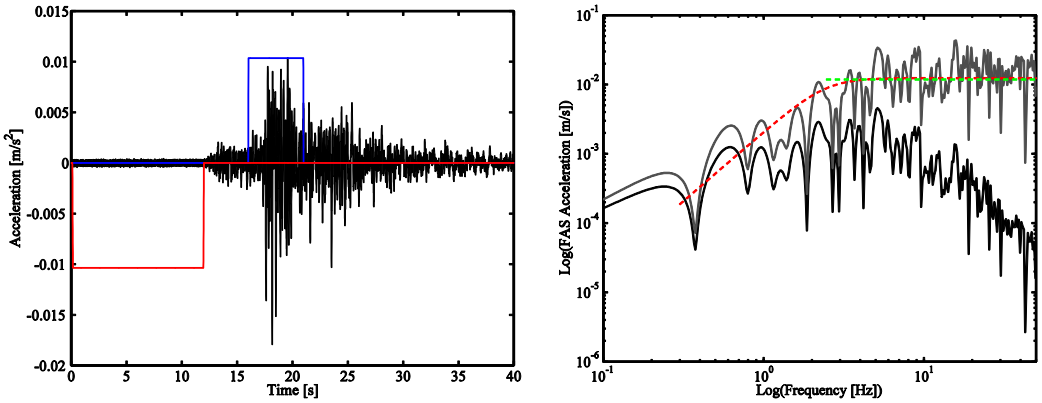

ID 11

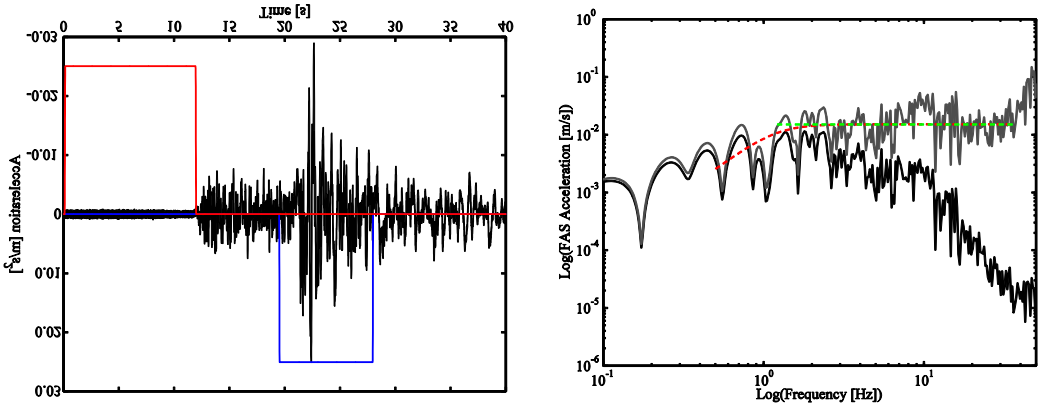

ID 14

Figure 2.3d. figure caption see Figure 2.3a.

We find it is critical to correct for path attenuation to obtain a stable estimate of f_C, the low-frequency asymptote and A_{rms}. With an accurate f_C, both the Brune spectral method and Hanks A_{rms} method give similar results for stress drop (Figure 2.4). We find tau-arms formulation (Equation (1.21)) to be valid for estimating stress drops at larger source-station distances (R ≤ 76 km) than found by Baltay et al. (2013). Although the data are corrected for Q, the variability in earthquake stress drop remains around a factor of 4—similar to what is found for global and regional seismic analyses. The factor of 4 is still about twice that expected from ground motion prediction equations (Cotton et al., 2013).

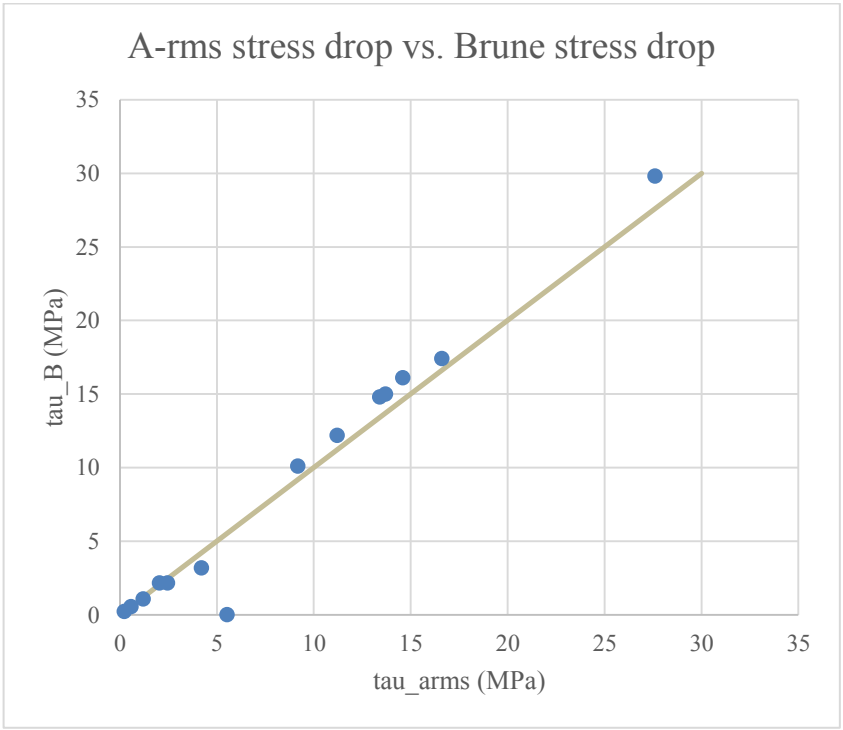

Figure 2.4: Comparison of Brune stress drop and Arms stress drop.

For these earthquakes we used a Q model of $Q = Q_0 f^a$. We find Q_0 between 40~120 and a around 0.1~0.5. After correcting for Q, the spectrum generally has an w^{-2} shape for frequencies up to 70 Hz for the close distances (and before the Nyquist

frequency of instrument) and up to 40 Hz (after which the noise affects the spectrum) for the far distances. This bandwidth allows for a stable estimate for f_C, the low-frequency asymptote (to determine seismic moment) and the rms acceleration.

Secondly, this analysis (data listed in Table 2.1) suggests that the intrinsic variability in earthquake stress drop is around a factor of 4. Using the Brune method we find the log-mean value of tau is 0.51 MPa for tau_B-Mag and 0.71 MPa and tau_B-f, with an uncertainty of a factor 4.9 and 3.8, respectively. The same spectra produce tau_A-rms of 0.49 MPa, with an uncertainty of a factor of 3.6. The mean value of stress drop is similar for both the Brune and A-rms method. The mean value of stress drop appears to be about 6 times smaller than the global average (Allmann and Shearer, 2009). However, the global average was based on a relationship between corner frequency and source radius (Madariaga, 1976) that by itself produces a stress drop that will be 5.5 times larger than predicted by the Brune relationship. Thus our results are close to the global average.

Thirdly, our analysis suggests that we can use the A_{rms} method for estimating tau for distances as large as 76 km provided we correct the spectrum for whole path attenuation.

3. Oklahoma

3.1 Stations and Data

In Figure 3.1, all the dark blue circles are epicenters prior to 2009. The others are color coded by year. The earthquakes we will talk about are near Guthrie –see lower left inset.

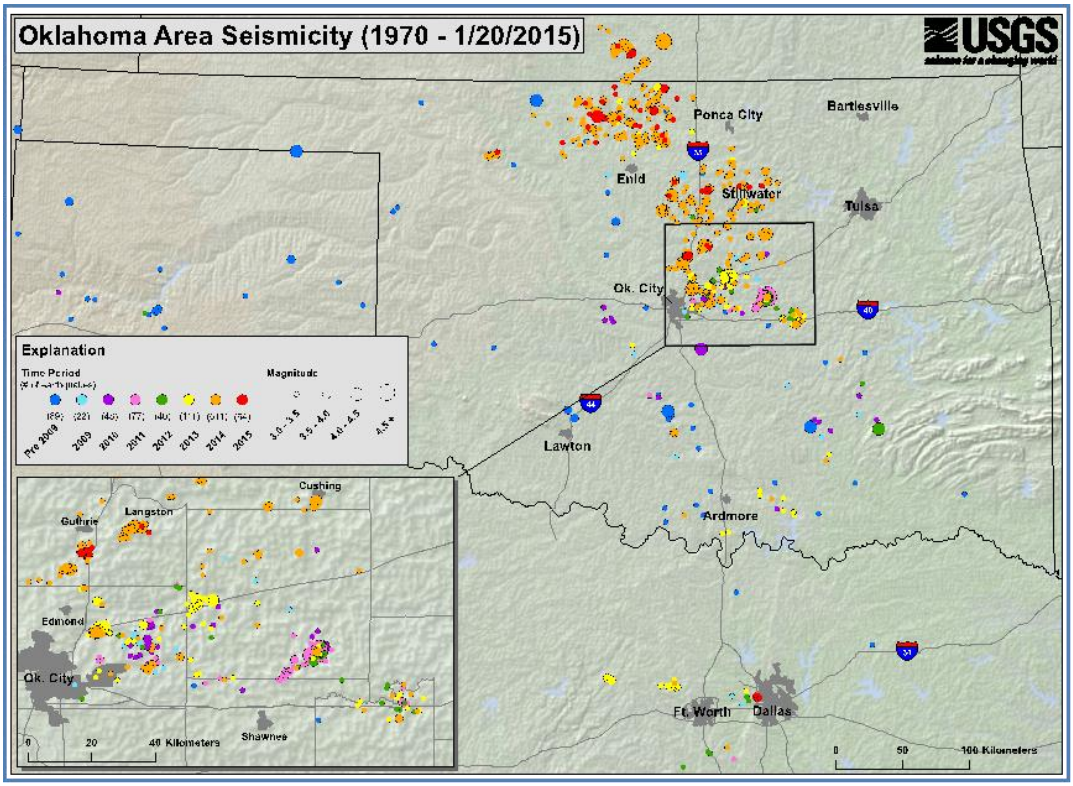

Figure 3.1. Map of the state of Oklahoma showing epicenters (colored dots) of earthquakes recorded from 1970 to 1/20/2015. Epicenters in Oklahoma. Inset is an enlargement that includes the area of interest for our study.

Another way to look at the number of earthquakes occurring in Oklahoma is shown in Figure 3.2. The number of earthquakes with M > 3 per year is more than those occurring in the entire western US. We want to know if the earthquakes in Oklahoma have stress

drops similar to other earthquakes, that is, will they create the same intensity of shaking for the same magnitude as we have seen in the western US.

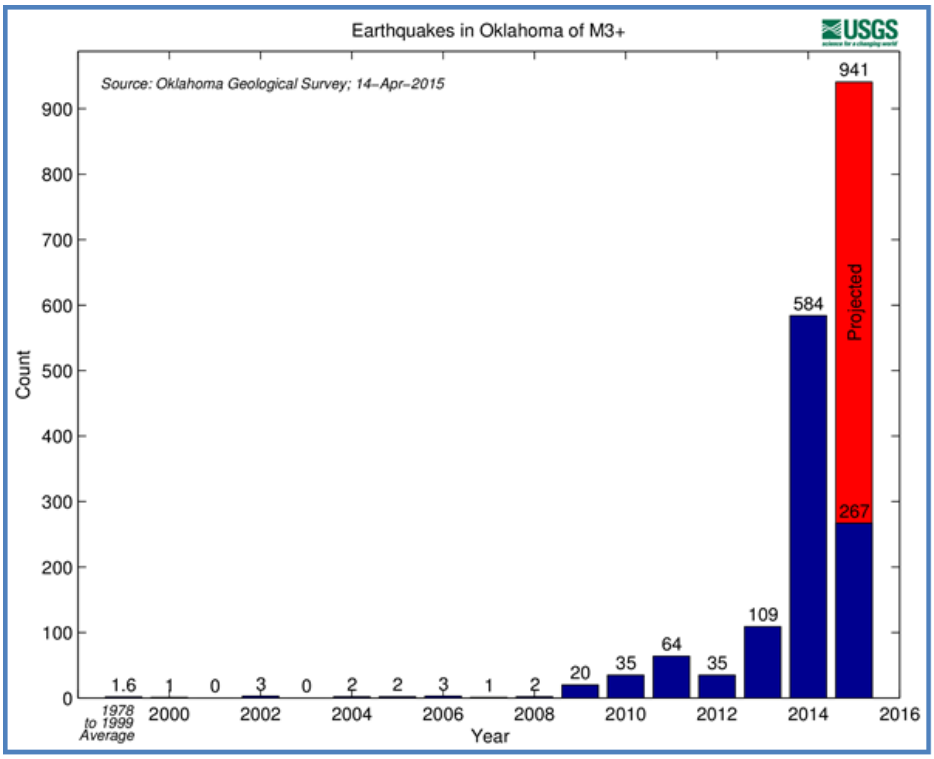

Figure 3.2. Number of earthquakes in Oklahoma with magnitudes greater than 3.

Within the central and eastern United States, the number of earthquakes has increased dramatically over the past few years. Between the years 1973–2008, there was an average of 21 earthquakes of magnitude three and larger in the central and eastern United States. This rate jumped to an average of 99 M3+ earthquakes per year in 2009–2013, and the rate continues to rise. In 2014, alone, there were 659 M3 and larger earthquakes. Most of these earthquakes are in the magnitude 3–4 range, large enough to have been felt by many people, yet small enough to rarely cause damage.

We use records from the following stations (Table 2): station OK025, OK026, OK027, OK028, OK029, OK030 and OK031 operated by US Geological Survey Network. The seismometer at these stations is the Trillium Compact Broadband Seismometer. And

station BCOK operated by Oklahoma Seismic Network uses the CMG-3ESP sensor. These are velocity sensors. After checking the specifications the records are all below the clip level, and the frequency range we study is not affected by the instrument response.

Table 2: Stations of Oklahoma

Station	Site	Latitude	Longitude	Elevation (m)	First start	Last end
OK025	Westminster Rd and Hefner Rd, NE Oklahoma City, Oklahoma, U.	35.5811	-97.3379	348	2013/12/18	2999/12/31
OK026	New Dominion Farley field, Oklahoma City, Oklahoma, U.S.A.	35.4153	-97.4514	398	2013/12/18	2015/3/3
OK027	Henny and Sorgum Hills Rd.	35.711956	-97.283642	364	2014/2/14	2015/3/3
OK028	N Oak Rd and Britton Rd, Lincoln County	35.56111	-97.061389	330	2014/2/18	2015/3/3
OK029	Liberty Lake, Oklahoma, USA	35.79657	-97.45486	333	2014/2/13	2999/12/31
OK030	Cody Creek RV Park, Cushing, OK, USA	35.92778	-96.78375	289	2014/10/16	2999/12/31
OK031	2598 S. Brethren Rd., Cushing, OK, USA	35.95309	-96.83911	290	2014/10/15	2999/12/31
BCOK	Bluff Creek, North Oklahoma City, Oklahoma	35.656729	-97.609276	302	2013/2/9	2599/12/31

We examine M>3 earthquake events within a square area (~10 km x 10 km) marked by latitudes (35.96, 35.86) and longitudes (-97.38, -97.25) in the period December 29, 2013 to June 30 2015. This results in 60 events (Figure 3.3). For each event, we study the data recorded by the 3~5 nearest stations within a distance of 55 km of the epicenters. This results in 262 source-station data in Oklahoma (Table 3).

What's more, as we could see from Figure 3.3, the 60 events locate in a relatively small area comparing to the source-station distance, which means that the source-station paths are relatively fixed. That implies that the path attenuation should not vary much

among the events for each specific station. This helps to increase the effectiveness of our method to remove path attenuation.

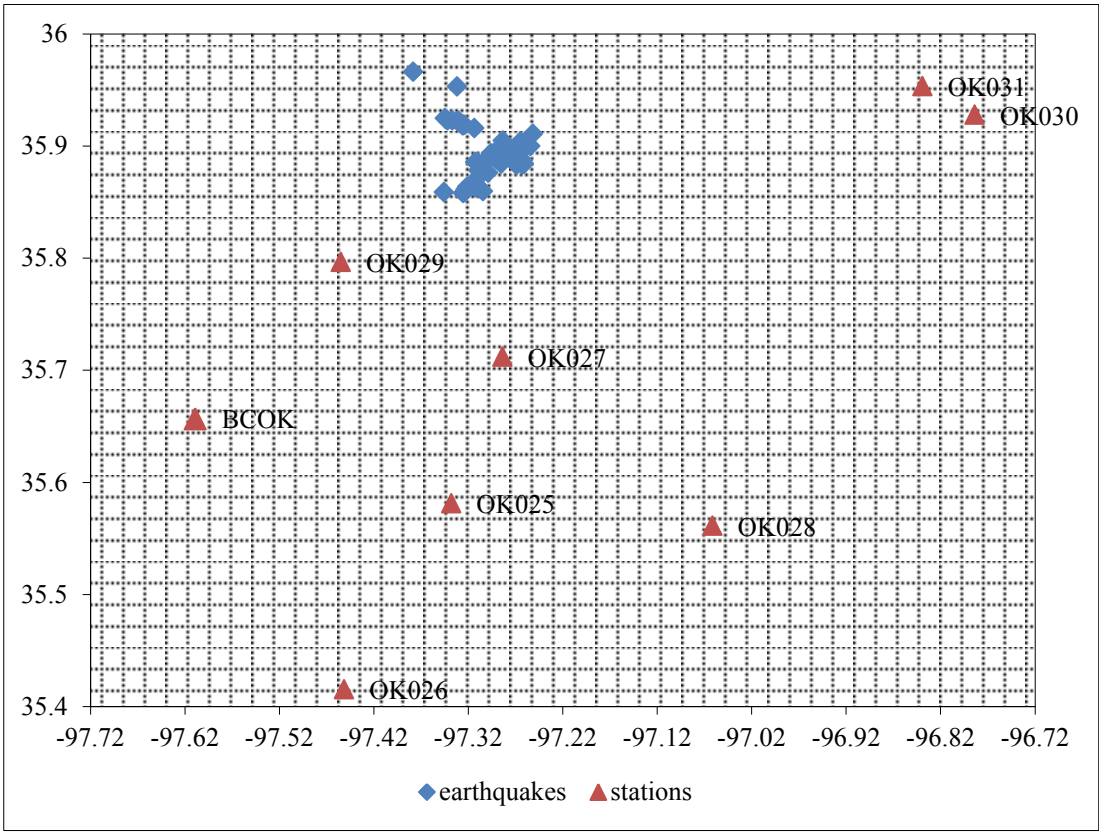

Figure 3.3. Map of stations and epicenters that we have analyzed in Oklahoma.

3.2 Method

As we did for analysis of earthquakes in central California, we assume a frequency-dependent Q model $Q = Q_0 f^{\alpha}$ for path attenuation. To find the parameters (Q_0, a) we fit the acceleration amplitude spectrum of the recorded S wave for each earthquake. We examine all 60 earthquakes rccorded by 3-5 stations, resulting in 262 source-station data, to get the Q_0 and a. These parameters are used to remove path attenuation from the spectrum for each specific record. Then assuming a Brune model as

the source spectrum, we fit each spectrum to determine the low-frequency asymptote Ω_0 and corner frequency f_C. We use both the low-frequency asymptote and the catalog magnitude to determine the seismic moment. With the seismic moment and corner frequency we use equation 1.1 to estimate the Brune stress drop,.

The steps in the method are almost the same as we used for central California:

(1) We isolate the SH time history recorded on the accelerometer. In steps, we remove the instrument response, remove the mean and convert from counts to physical units. Then we rotate the horizontal components to get the transverse component, and isolate the SH component of the shear wave. We apply a cosine taper of 0.5% to the isolated waveform to smoothly decrease the amplitude to zero at both ends of the waveform.

(2) We estimate Q for the path. In this step, we Fourier Transform (FT) the tapered data, plot the spectrum in the log(A)-f format (log-linear), and find a curve that fits this plot using the equation $y = a + bf^{1-a}$. Then we use the slope value (b) and travel time value to calculate Q_0 and α.

(3) Correct FAS for path attenuation using results from step (2).

(4) Fit the corrected source spectrum with a function that is the idealized Brune spectrum to find the corner frequency (f_C) and low-frequency asymptote (Ω_0) using the following equation:

$$D = \frac{\Omega}{1 + (\frac{f}{fc})^2}$$

(5) Estimate the stress drop from equation 1.1. Here, we estimate the Brune stress drop using seismic moment from two methods: in the first one we use the catalog magnitude (Mag) to get seismic moment (M_0) in the following equation:

$$M_0 = 10^{9.1+1.5M}$$

The second method is to use W_0 (the low-frequency asymptote of the displacement spectrum) to estimate M_0:

$$M_0 = 4\pi\rho b^3 R \cdot W_0$$

R is the distance from source to station. We use tau_B to represent the catalog magnitude Brune method stress drop, and tau_B_spec as the spectral W_0-moment method Brune stress drop.

(7) We lowpass filter (corner is usually 30Hz or 40Hz) to filter the high frequency inaccurate spectrum, because the antialias frequency exist and therefore the high frequencies wouldn't get an reasonable results after step (3), as the same seen in Figure 2.3. We do an inverse FFT to the Q-corrected spectrum. Then we use a time window with a length of 1.5s to get the maximum root-mean-square value of the acceleration a_{rms}. We use this value in equation (1.19) to get tau_arms.

3.3 Results and Discussion

The mean value of Brune stress drop using the spectral determined magnitude is 0.433 MPa, with a multiplicative uncertainty of 4.52. The mean value of Brune stress drop using network magnitude is 0.38 MPa, with a multiplicative uncertainty of 3.12. The mean value of A_{rms} (from the time domain estimate of A_{rms} with a window length of 1.5s) stress drop is 1.04 MPa, with a multiplicative uncertainty of 1.79. The uncertainty of A_{rms} is much lower than that determined for the Brune stress drop. Table 3 shows the Brune stress drops for the 60 events using the spectral determined magnitude, while Table 4 shows the A_{rms} stress drops using a window length of 1.5s for the same 60 events.

Table 3: tau_B of Oklahoma earthquakes

ID	Date	Mag	Depth (km)	OK025	OK026	OK027	OK028	OK029	OK030	OK031	BCOK
1	2013/12/29	mwr37	5	0.05	0.01	-	-	-	-	-	-
2	2014/2/9	mwr41	5	0.09	0.02	-	-	-	-	-	-
3	2014/3/8	ml30	4.7	0.27	-	0.04	0.02	0.04	-	-	-
4	2014/3/8	ml31	5	0.16	-	0.21	0.13	0.71	-	-	0.43
5	2014/3/11	mwr34	4.9	2.82	-	0.20	1.04	0.48	-	-	0.25
6	2014/3/17	ml31	5.1	0.50	-	0.11	0.29	0.25	-	-	0.25
7	2014/3/20	ml33	5	0.47	-	0.21	0.26	0.92	-	-	0.67
8	2014/3/22	ml30	5	1.14	-	0.39	1.73	0.47	-	-	0.53
9	2014/3/22	ml31	4.5	0.22	-	0.38	0.09	0.07	-	-	0.41
10	2014/3/22	ml31	4.5	1.10	-	1.05	0.65	0.19	-	-	0.28
11	2014/3/22	mwr39	4.5	0.50	-	0.33	0.66	0.52	-	-	2.25
12	2014/3/27	ml32	4.6	0.69	-	0.24	0.07	0.53	-	-	-
13	2014/3/31	ml30	5	0.09	-	0.08	0.06	0.05	-	-	-
14	2014/4/1	ml32	5	0.39	-	0.23	0.39	0.28	-	-	-
15	2014/4/3	ml33	4.8	0.55	-	0.20	0.26	0.15	-	-	-
16	2014/4/4	ml30	4.2	0.12	-	0.09	0.43	0.13	-	-	-
17	2014/4/4	ml31	5	0.12	-	0.11	0.22	0.11	-	-	-
18	2014/4/4	ml34	5	0.27	-	0.12	0.20	0.28	-	-	-
19	2014/4/4	ml35	5.2	0.91	-	0.27	0.30	0.34	-	-	-
20	2014/4/6	ml30	5	0.52	-	0.15	0.29	0.14	-	-	-
21	2014/4/7	ml31	5.3	0.23	-	0.25	0.10	0.46	-	-	-
22	2014/4/7	ml31	5	1.66	-	0.23	0.43	0.49	-	-	-
23	2014/4/7	mwr42	5.1	2.55	-	1.45	1.38	3.80	-	-	-
24	2014/4/9	ml32	4.7	0.63	-	0.26	0.23	0.54	-	-	-
25	2014/4/11	ml30	5.1	0.24	-	0.09	0.37	0.20	-	-	-
26	2014/4/12	ml33	3.1	1.76	-	0.27		0.33	-	-	0.38
27	2014/5/2	ml30	6.4	1.92	-	0.66	0.52	1.28	-	-	3.75
28	2014/5/6	ml32	4.8	0.67	-	0.69	0.24	0.20	-	-	0.83

ID	Date	Mag	Depth (km)	OK025	OK026	OK027	OK028	OK029	OK030	OK031	BCOK
29	2014/5/21	mb_lg30	7.4	0.67	-	0.68	0.29	0.24	-	-	1.55
30	2014/6/26	ml38	5	0.64	-	0.68	0.82	0.53	-	-	2.30
31	2014/6/27	ml33	5.5	2.69	-	0.82	0.82	1.09	-	-	9.78
32	2014/6/27	ml35	4.8	0.48	-	0.69	0.75	0.26	-	-	0.84
33	2014/6/27	mwr36	5	2.57	-	4.69	1.33	1.15	-	-	3.43
34	2014/6/30	ml32	4.5	1.09	-	0.44	0.68	0.51	-	-	4.22
35	2014/7/12	ml31	5	0.14	-	0.16	0.05	0.15	-	-	0.21
36	2014/7/12	ml32	5	0.25	-	0.30	0.12	0.17	-	-	0.16
37	2014/7/12	mwr4	4	1.03	-	1.23	0.48	0.92	-	-	1.30
38	2014/7/13	ml30	4.8	0.06	-	0.17	0.03	0.09	-	-	0.12
39	2014/7/14	ml33	5.1	0.32	-	1.02	0.37	0.36	-	-	0.29
40	2014/7/23	ml31	5	0.77	-	2.01	0.30	0.35	-	-	0.76
41	2014/7/23	ml32	5.1	0.92	-	3.12	0.67	0.71	-	-	5.71
42	2014/7/23	mwr33	5.3	1.59	-	0.61	0.52	0.95	-	-	2.41
43	2014/8/14	ml32	5.1	0.52	-	0.40	0.13	1.25	-	-	1.45
44	2014/8/20	ml30	5	0.47	-	0.11	0.16	0.14	-	-	10.83
45	2014/8/20	ml31	4.5	0.20	-	0.09	0.40	0.20	-	-	0.23
46	2014/8/20	ml33	4.9	0.61	-	0.24	0.48	0.17	-	-	1.21
47	2014/10/25	ml31	5	0.27	-	-	0.10	0.13	-	-	0.40
48	2014/10/31	ml32	4.5	1.04	-	0.69	-	1.42	-	0.30	1.33
49	2014/12/4	ml31	5	0.31	-	-	0.17	-	-	1.40	-
50	2014/12/27	ml30	4.8	0.45	-	-	-	-	0.17	1.29	-
51	2015/1/17	ml32	6.9	0.88	-	1.18	-	0.80	-	2.95	0.76
52	2015/2/8	ml31	6	0.35	-	-	0.08	0.12	-	0.08	-
53	2015/2/19	ml31	2.2	0.32	-	0.18	-	0.51	-	0.18	0.39
54	2015/4/17	mb_lg31	5.7	0.29	-	-	-	0.25	-	0.63	0.84
55	2015/4/17	mb_lg33	7.6	1.14	-	-	-	0.91	-	1.34	1.89
56	2015/4/17	mb_lg38	5.8	0.91	-	-	-	1.03	-	1.33	-
57	2015/4/17	mb_lg39	6.5	1.00	-	-	-	0.72	-	1.55	-
58	2015/4/19	mb_lg39	7.9	0.98	-	-	-	1.11	-	2.67	-
59	2015/4/19	mb41	7.6	0.76	-	-	-	0.03	-	0.39	0.05
60	2015/4/27	mwr41	4.2	0.04	-	-	-	0.12	-	0.16	0.14

Table 4: A-rms stress drop using 1.5s time window

ID	Date	Mag	Depth (km)	OK025	OK026	OK027	OK028	OK029	OK030	OK031	BCOK
1	2013/12/29	mwr37	5	0.59	0.24	-	-	-	-	-	-
2	2014/2/9	mwr41	5	0.45	0.22	-	-	-	-	-	-
3	2014/3/8	ml30	4.7	1.44	-	0.57	1.47	0.49	-	-	-
4	2014/3/8	ml31	5	1.09	-	1.12	1.66	1.66	-	-	2.19
5	2014/3/11	mwr34	4.9	1.61	-	0.77	2.82	1.13	-	-	0.76
6	2014/3/17	ml31	5.1	3.37	-	1.11	2.05	0.86	-	-	1.28
7	2014/3/20	ml33	5	0.99	-	0.98	1.51	1.25	-	-	1.18
8	2014/3/22	ml30	5	3.74	-	2.23	-	1.59	-	-	1.43
9	2014/3/22	ml31	4.5	1.31	-	2.17	1.28	0.79	-	-	2.04
10	2014/3/22	ml31	4.5	2.84	-	2.31	3.23	0.81	-	-	1.04
11	2014/3/22	mwr39	4.5	0.35	-	0.42	1.19	0.66	-	-	0.59
12	2014/3/27	ml32	4.6	1.85	-	1.42	1.13	1.24	-	-	-
13	2014/3/31	ml30	5	0.70	-	0.92	1.07	0.54	-	-	-
14	2014/4/1	ml32	5	1.06	-	1.00	2.51	0.78	-	-	-
15	2014/4/3	ml33	4.8	1.50	-	1.02	1.50	0.40	-	-	-
16	2014/4/4	ml30	4.2	1.36	-	1.36	2.08	0.83	-	-	-
17	2014/4/4	ml31	5	0.59	-	0.82	1.14	0.83	-	-	-
18	2014/4/4	ml34	5	0.75	-	0.81	1.31	0.88	-	-	-
19	2014/4/4	ml35	5.2	1.76	-	1.54	1.06	0.61	-	-	-
20	2014/4/6	ml30	5	2.82	-	1.55	1.59	0.70	-	-	-
21	2014/4/7	ml31	5.3	1.28	-	1.41	1.34	1.52	-	-	-
22	2014/4/7	ml31	5	2.48	-	1.25	2.08	1.25	-	-	-
23	2014/4/7	mwr42	5.1	0.72	-	0.51	0.82	0.41	-	-	-
24	2014/4/9	ml32	4.7	1.08	-	1.10	0.94	0.78	-	-	-
25	2014/4/11	ml30	5.1	1.55	-	1.00	-	1.23	-	-	0.79
26	2014/4/12	ml33	3.1	3.42	-	1.57	-	0.75	-	-	0.72
27	2014/5/2	ml30	6.4	3.90	-	3.46	3.45	1.36	-	-	0.75
28	2014/5/6	ml32	4.8	1.47	-	2.30	1.83	0.80	-	-	1.13
29	2014/5/21	mb_lg30	7.4	1.84	-	1.89	1.00	0.80	-	-	2.35
30	2014/6/26	ml38	5	0.40	-	0.60	1.23	0.55	-	-	1.39
31	2014/6/27	ml33	5.5	1.66	-	1.65	1.65	1.20	-	-	3.95
32	2014/6/27	ml35	4.8	0.63	-	0.97	1.73	0.76	-	-	1.02
33	2014/6/27	mwr36	5	1.03	-	1.38	1.51	0.72	-	-	1.35
34	2014/6/30	ml32	4.5	1.32	-	1.48	2.21	1.31	-	-	1.29
35	2014/7/12	ml31	5	0.76	-	1.07	0.50	0.46	-	-	0.73

ID	Date	Mag	Depth (km)	OK025	OK026	OK027	OK028	OK029	OK030	OK031	BCOK
36	2014/7/12	ml32	5	0.71	-	0.77	0.93	0.63	-	-	0.55
37	2014/7/12	mwr4	4	0.34	-	0.45	0.35	0.28	-	-	0.40
38	2014/7/13	ml30	4.8	0.53	-	0.85	0.50	0.62	-	-	0.50
39	2014/7/14	ml33	5.1	0.50	-	0.87	0.90	0.69	-	-	0.36
40	2014/7/23	ml31	5	1.21	-	0.74	1.09	0.81	-	-	1.27
41	2014/7/23	ml32	5.1	1.37	-	0.98	2.61	1.51	-	-	1.88
42	2014/7/23	mwr33	5.3	1.03	-	0.92	1.21	1.07	-	-	1.54
43	2014/8/14	ml32	5.1	0.81	-	1.28	0.88	1.28	-	-	1.19
44	2014/8/20	ml30	5	1.20	-	0.81	1.59	1.01	-	-	2.42
45	2014/8/20	ml31	4.5	0.70	-	0.60	2.77	0.96	-	-	0.76
46	2014/8/20	ml33	4.9	0.63	-	0.75	1.88	0.85	-	-	1.57
47	2014/10/25	ml31	5	1.01	-	-	0.63	0.33	-	-	0.69
48	2014/10/31	ml32	4.5	2.41	-	3.40	-	2.21	-	2.40	2.33
49	2014/12/4	ml31	5	0.88	-	-	1.09	-	-	1.82	-
50	2014/12/27	ml30	4.8	1.39	-	-	-	-	1.45	1.68	-
51	2015/1/17	ml32	6.9	1.94	-	2.25	-	2.16	-	1.36	1.95
52	2015/2/8	ml31	6	2.04	-	-	0.88	0.37	-	-	0.52
53	2015/2/19	ml31	2.2	0.59	-	0.76	-	0.57	-	0.89	0.58
54	2015/4/17	mb_lg31	5.7	0.92	-	-	-	0.79	-	1.93	1.22
55	2015/4/17	mb_lg33	7.6	1.43	-	-	-	1.09	-	2.17	1.34
56	2015/4/17	mb_lg38	5.8	0.47	-	-	-	0.41	-	0.68	-
57	2015/4/17	mb_lg39	6.5	0.49	-	-	-	0.27	-	0.83	-
58	2015/4/19	mb_lg39	7.9	0.59	-	-	-	0.59	-	1.39	-
59	2015/4/19	mb41	7.6	0.30	-	-	-	0.24	-	0.76	0.37
60	2015/4/27	mwr41	4.2	0.25	-	-	-	0.39	-	0.56	0.54

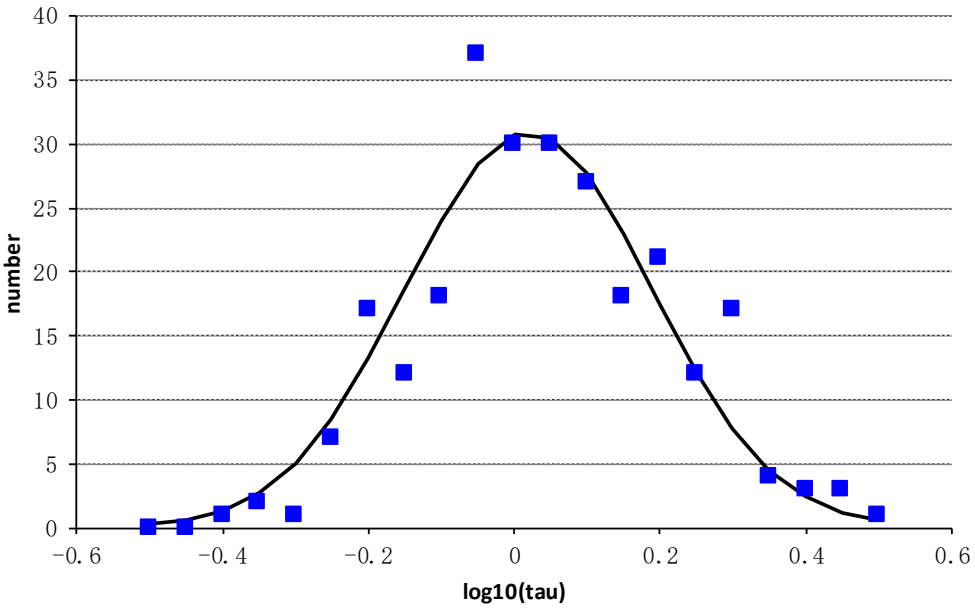

Figure 3.4. The black line is the normal distribution, and the blue dots show the histogram values of log10(tau_arms) equally spaced bins in log10 space..

4. Conclusion

We find tau-arms formulation (Equation 1.19) to be valid for estimating stress drops at larger source-station distances (R ≤ 76 km) than used by Baltay et al. (2014). It is critical to correct for path attenuation for a stable estimate f_C, the low-frequency asymptote and a-rms. This analysis also suggests that the variability in earthquake stress drop is around a factor of 4 if one uses a Brune stress drop computed by corner frequency and seismic moment. However, stress drop estimated by A_{rms} computed in the time domain, after accounting for attenuation, gives a stable stress drop with a much lower uncertainty—a multiplicative factor around 2.0. That uncertainty is comparable to that found from GMPE's (Cotton et al., 2015).

Reference

Aki, K. (1967). Scaling law of seismic spectrum, *J. Geophys. Res.* 72, 1217–1231.

Al Atik, L., N. Abrahamson, J. J. Bommer, F. Scherbaum, F. Cotton, and N. Kuehn (2010). The variability of ground-motion prediction models and its components, *Seismol. Res. Lett.* 81, no. 5, 794–801.

Anderson, J. G. (1986). Implication of attenuation for studies of the earthquake source. *Earthquake Source Mechanics*, 311-318.

Anderson, J. G., and S. E. Hough (1984). A model for the shape of the Fourier amplitude spectrum of acceleration at high frequencies, *Bull. Seismol. Soc. Am.* 74, no. 5, 1969–1993.

Archuleta, R. J., E. Cranswick, C. Mueller, and P. Spudich (1982). Source parameters of the 1980 Mammoth Lakes, California, earthquake sequence, *J. Geophys. Res.* 87, 4595–4607.

Baltay, A. S., Hanks, T. C., & Beroza, G. C. (2013). Stable stress‐drop measurements and their variability: Implications for ground‐motion prediction. *Bull. Seismol. Soc. Am.,* 103(1), 211-222.

Boore, D. M. (2012). Updated determination of stress parameters for several well-recorded earthquakes in Eastern North America, *Seismol. Res. Lett.* 83, 190-199.

Brune, J. N. (1970). Tectonic stress and the spectra of seismic shear waves from earthquakes, *J. Geophys. Res.* 75, no. 26, 4997–5009.

Cotton, F., Archuleta, R., & Causse, M. (2013). What is sigma of the stress drop? , *Seismol. Res. Lett.,* 84(1), 42-48.

Graves, R. A. Pitarka (2010). Broadband ground motion simulation using hybrid approach, *Bull. Seism. Soc. Am.*, 100, 5A, 2095-2123.

Hanks, T. C. (1982). fmax, *Bull. Seismol. Soc. Am.* 72, 1867–1879.

Hanks, T. C. (1979). b-values and ω-γ seismic source models: Implications for tectonic stress variations along active crustal fault zones and the estimation of high-frequency strong ground motion, *J. Geophys. Res.* 84, 2235–2242.

Irikura, K. and H. Miyake (2010). Recipe for predicting strong ground motion from crustal earthquake scenarios, *Pure. Appl. Geophys.*, doi: 10.1007/s00024-010-0150-9.

Mena, B. and Mai, P. M., Olsen, K. B., Purvance, M. D. and Brune, J. N. (2010). Hybrid broadband ground-motion simulation using scattering Green's functions: Application to large-magnitude events, *Bull. Seism. Soc. Am.* 100, 2143-2162.

Motzzedian, D. and G. M. Atkinson (2005). Stochastic finite-fault modeling based on a dynamic corner frequency, *Bull. Seismol. Soc. Am.* 95, 995-1010.

Oth, A., D. Bindi, S. Parolai, and D. Di Giacomo (2010). Earthquake scaling characteristics and the scale-(in)dependence of seismic energy-to-moment ratio: Insights from KiK-net data in Japan, *Geophys. Res. Lett.* 37, L19304, doi: 10.1029/2010GL044572.

Shearer, P. M., G. A. Prieto, and E. Hauksson (2006). Comprehensive analysis of earthquakes source spectra in southern California, *J. Geophys. Res.* 111, doi: 10.1029/2005JB003979.

Schmedes, J., R. J. Archuleta, and D. Lavallée (2013). A kinematic rupture model generator incorporating spatial interdependency of earthquake source parameters, *Geophys. J. Int.* 192 **(3),** 1116-1131. doi: 10.1093/gji/ggs02.

Sonley, E., and R. E. Abercrombie (2006). Effects of methods of attenuation correction on source parameter determination, in Earthquakes: Radiated Energy and the

Physics of Faulting, *Geophysical Monograph-American Geophysical Union* 170 (2006): 91.

Sonley., R. Abercrombie et al., (Editors), Vol. 170, AGU, Washington, DC, 91–97.

Zeng, Y., J. G. Anderson and G. Yu (1994). A composite source model for computing realistic synthetic strong ground motions, *Geophysical Research Letters* 21, 725-728.

Appendix A

Table: tau_arms_1/fc

ID	Date	Mag	Depth (km)	OK025	OK026	OK027	OK028	OK029	OK030	OK031	BCOK
1	2013/12/29	mwr37	5	0.57	0.24	-	-	-	-	-	-
2	2014/2/9	mwr41	5	0.45	0.22	-	-	-	-	-	-
3	2014/3/8	ml30	4.7	0.95	-	0.50	1.39	0.47	-	-	-
4	2014/3/8	ml31	5	0.73	-	0.77	1.50	1.07	-	-	1.44
5	2014/3/11	mwr34	4.9	0.76	-	0.60	2.46	0.79	-	-	0.61
6	2014/3/17	ml31	5.1	1.87	-	0.73	1.58	0.59	-	-	0.98
7	2014/3/20	ml33	5	0.64	-	0.63	1.43	0.96	-	-	0.97
8	2014/3/22	ml30	5	1.41	-	1.05	0.00	1.14	-	-	0.95
9	2014/3/22	ml31	4.5	0.91	-	1.68	1.20	0.53	-	-	1.56
10	2014/3/22	ml31	4.5	1.52	-	1.05	2.69	0.60	-	-	0.60
11	2014/3/22	mwr39	4.5	0.33	-	0.36	0.98	0.56	-	-	0.42
12	2014/3/27	ml32	4.6	1.14	-	0.92	0.95	0.75	-	-	-
13	2014/3/31	ml30	5	0.51	-	0.56	1.03	0.52	-	-	-
14	2014/4/1	ml32	5	0.62	-	0.75	2.08	0.55	-	-	-
15	2014/4/3	ml33	4.8	0.85	-	0.67	1.32	0.33	-	-	-
16	2014/4/4	ml30	4.2	0.75	-	0.74	1.72	0.65	-	-	-
17	2014/4/4	ml31	5	0.39	-	0.53	1.06	0.79	-	-	-
18	2014/4/4	ml34	5	0.51	-	0.61	1.20	0.76	-	-	-
19	2014/4/4	ml35	5.2	0.98	-	1.22	0.99	0.56	-	-	-
20	2014/4/6	ml30	5	1.28	-	1.00	1.33	0.47	-	-	-
21	2014/4/7	ml31	5.3	0.93	-	0.98	0.87	0.84	-	-	-
22	2014/4/7	ml31	5	1.19	-	0.75	1.70	0.89	-	-	-
23	2014/4/7	mwr42	5.1	0.50	-	0.45	0.78	0.36	-	-	-
24	2014/4/9	ml32	4.7	0.65	-	0.81	0.60	0.42	-	-	-
25	2014/4/11	ml30	5.1	0.81	-	0.66	-	0.87	-	-	0.52
26	2014/4/12	ml33	3.1	1.64	-	1.10	-	0.56	-	-	0.59
27	2014/5/2	ml30	6.4	1.83	-	1.61	2.51	0.87	-	-	0.40
28	2014/5/6	ml32	4.8	0.87	-	1.66	1.23	0.43	-	-	0.70
29	2014/5/21	mb_lg30	7.4	1.28	-	1.49	0.68	0.55	-	-	1.41
30	2014/6/26	ml38	5	0.34	-	0.50	0.71	0.37	-	-	0.90
31	2014/6/27	ml33	5.5	0.77	-	1.23	0.84	0.63	-	-	1.76
32	2014/6/27	ml35	4.8	0.47	-	0.76	1.37	0.55	-	-	0.76
33	2014/6/27	mwr36	5	0.67	-	1.03	1.03	0.50	-	-	0.71
34	2014/6/30	ml32	4.5	0.78	-	0.99	1.32	0.79	-	-	0.53

35	2014/7/12	ml31	5	0.64	-	0.79	0.45	0.36	-	-	0.58
36	2014/7/12	ml32	5	0.61	-	0.56	0.72	0.43	-	-	0.43
37	2014/7/12	mwr4	4	0.28	-	0.34	0.35	0.22	-	-	0.34
38	2014/7/13	ml30	4.8	0.42	-	0.40	0.49	0.41	-	-	0.34
39	2014/7/14	ml33	5.1	0.32	-	0.53	0.83	0.60	-	-	0.26
40	2014/7/23	ml31	5	0.73	-	0.53	0.65	0.44	-	-	0.76
41	2014/7/23	ml32	5.1	0.87	-	0.61	1.41	0.80	-	-	0.82
42	2014/7/23	mwr33	5.3	0.59	-	0.66	0.68	0.54	-	-	0.84
43	2014/8/14	ml32	5.1	0.53	-	0.73	0.70	0.79	-	-	0.65
44	2014/8/20	ml30	5	0.68	-	0.56	0.84	0.55	-	-	0.70
45	2014/8/20	ml31	4.5	0.55	-	0.54	1.68	0.71	-	-	0.55
46	2014/8/20	ml33	4.9	0.42	-	0.60	1.04	0.66	-	-	0.91
47	2014/10/25	ml31	5	0.73	-	-	0.55	0.33	-	-	0.69
48	2014/10/31	ml32	4.5	1.11	-	2.08	-	1.62	-	1.63	1.86
49	2014/12/4	ml31	5	0.59	-	-	0.83	-	-	1.12	-
50	2014/12/27	ml30	4.8	0.76	-	-	-	-	0.76	0.77	-
51	2015/1/17	ml32	6.9	1.11	-	1.84	-	1.36	-	0.93	1.03
52	2015/2/8	ml31	6	1.14	-	-	0.62	0.22	-	-	0.36
53	2015/2/19	ml31	2.2	0.38	-	0.47	-	0.39	-	0.59	0.50
54	2015/4/17	mb_lg31	5.7	0.67	-	-	-	0.53	-	1.07	0.68
55	2015/4/17	mb_lg33	7.6	0.84	-	-	-	0.70	-	1.23	0.83
56	2015/4/17	mb_lg38	5.8	0.13	-	-	-	0.10	-	0.19	-
57	2015/4/17	mb_lg39	6.5	0.26	-	-	-	0.09	-	0.10	-
58	2015/4/19	mb_lg39	7.9	0.36	-	-	-	0.41	-	0.44	-
59	2015/4/19	mb41	7.6	0.56	-	-	-	0.27	-	0.71	0.38
60	2015/4/27	mwr41	4.2	0.26	-	-	-	0.39	-	0.55	0.54